The role of gravity or pressure and contact stiffness in granular rheology

New Journal of Physics
The open access journal at the forefront of physics

Deutsche Physikalische Gesellschaft DPG
IOP Institute of Physics

Published in partnership with: Deutsche Physikalische Gesellschaft and the Institute of Physics

OPEN ACCESS

RECEIVED
27 November 2014

REVISED
23 February 2015

ACCEPTED FOR PUBLICATION
9 March 2015

PUBLISHED
15 April 2015

PAPER

The role of gravity or pressure and contact stiffness in granular rheology

Abhinendra Singh, Vanessa Magnanimo, Kuniyasu Saitoh and Stefan Luding

Multi Scale Mechanics (MSM), MESA +, CTW, University of Twente, PO Box 217, 7500 AE Enschede, The Netherlands

E-mail: a.singh-1@utwente.nl

Keywords: granular flow, rheology, granular solids

Abstract

The steady-state shear rheology of granular materials is investigated in slow quasistatic and inertial flows. The effect of gravity (thus the local pressure) and the often-neglected contact stiffness are the focus of this study. A series of particle simulations are performed on a weakly frictional granular assembly in a split-bottom geometry considering various magnitudes of gravity and contact stiffnesses. While traditionally the inertial number, i.e., the ratio of stress to strain-rate time scales, is used to describe the flow rheology, we report that a second dimensionless number, the ratio of softness and stress time scales, must also be included to characterize the bulk flow behavior. For slow, quasistatic flows, the density increases while the effective (macroscopic) friction decreases with increase in either particle softness or local pressure. This trend is added to the $\mu(I)$ rheology and can be traced back to the anisotropy in the contact network, displaying a linear correlation between the effective friction coefficient and deviatoric fabric in the steady state. When the external rotation rate is increased towards the inertial regime, for a given gravity field and contact stiffness, the effective friction increases faster than linearly with the deviatoric fabric.

1. Introduction

Granular media are envisaged as a collection of macroscopic and athermal particles which interact through dissipative contact forces [1–3]. A continuum description of the flow behavior of granular media is highly desirable, due to its application in both natural phenomena and industrial applications [1, 2]. Despite the numerous efforts, the constitutive relations describing the granular flow behavior is still a matter of debate. Solid mechanics and kinetic theory have been successful in predicting the solid–and gas–like behavior respectively [4, 5]. At one extreme particles interact via enduring contacts, while in the gaseous regime the binary collisions are the mode of momentum exchange. The recently proposed inertial number framework has been successful in describing the flow behavior in the liquid like regime when the particles not only undergo collisions but also frictional interactions with other particles [3, 6–8]. Though it very well predicts the flow behavior in case of homogeneous shear, it fails in case of a non-homogeneous shear flow [9–11].

Gravity (compression) is a critical factor in many granular flows [1, 3, 8]. Avalanches and debris flows play an important role in the transport of mass existing at the surface of Earth. Gravity-driven flows have also been observed on other planetary bodies of our solar system and are of particular importance in understanding the geology of planets and asteroids as well as for the human exploration of the Moon and Mars in the coming decades [12]. Currently, surface features found on Mars [13], Venus [14], and the Moon [15] are hypothesized to be the results of avalanches of granular material.

One of the important aspects of granular shear flows is the dependence of stress on imposed driving rate. Various experimental and numerical studies have shown that for slow–dense, quasistatic flows, the ratio of shear to compressive stress (*effective friction coefficient*) is independent of the imposed driving rate [3, 16, 17]. However, very little is known regarding the same in the presence of a broader range of normal stress. Shear tests performed on parabolic flights have shown an increase in the effective friction at low confinement [18–23].

Brucks *et al* [24] also obtained a similar trend using centrifuge experiments at gravity levels larger than Earth's gravity. Despite these studies, the effect of external compression (gravity) on granular flows is still poorly understood.

Soft materials like hydrogel and elastomer, which can support large deformation are of increasing importance in engineering and biological applications such as tissue scaffolding, bioseparation and micro-and-nano–printing [25]. While inertial number has been relatively successful in understanding the dynamics of rigid particles [6], elasticity becomes relevant for soft particles [17, 26]. The deformability of the soft particles has been shown to affect the force network close to the jamming transition [27]. Recent study by Vaart *et al* [28] has shown different rheological behavior for hard and soft particle suspensions. Despite the increasing importance, the models for soft deformable particles have been largely ignored, and only recently in a few theoretical attempts have been made to incorporate the particle stiffness [29, 30].

We claim here that these two factors, i.e., pressure (gravity) and softness can be seen as two aspects of the same phenomenon. We aim to test this claim by answering the following questions: (1) How does particle softness affect the bulk flow behavior? (2) Is there a unique law that can describe the flow behavior on Earth, Mars, and the Moon, i.e., for a broad range of pressure?

In this paper, we address the preceding questions with a focus on dense, weakly frictional, quasistatic granular flow. Using the discrete element method (DEM), we simulate cohesionless frictional granular material in a split-bottom ring shear cell. An important aspect of this setup is that the shear rate is given solely by external rotation rate and the geometry. At the same time, in this geometry the local strain rate does not depend strongly on the external compression [31], unlike the inclined plane and rotation drum where gravity has a strong effect [24, 32, 33]. To study the effect of pressure (gravity) and particle softness, we independently vary both gravity and particle softness by two orders of magnitude. In order to scan wide range of pressure in our set up, we manipulate the gravity field. A change in particle softness provides an adjustment on the microscopic scale, while gravity is a macroscopic (field) modification. We find that they have similar effect at the mesoscopic (local) scale. The bulk behavior can be well described using a dimensionless parameter, defined as the ratio between the time scales due to gravitational compression and contact stiffness. Furthermore, by increasing the external rotation rate, we study the dependence of effective friction and contact network anisotropy (deviatoric fabric) on the inertial number. The dependence of effective friction and deviatoric fabric on pressure is added to $\mu(I)$ rheology. Finally, we address the non-local effects in our results due to the presence of gradients in both stress and strain rate, which are quantified by following an approach similar to Koval *et al* [9].

The outline of this paper is as follows: in section 2 we describe our numerical setup and methodology. We present our results for quasistatic state in section 3. In section 4, we provide results on the rheological behavior and combine it with the results from quasistatic state to present new rheological laws. We then close the paper with a discussion of our results in section 5 along with a possible outlook for future research.

2. Discrete element method (DEM)

2.1. Model

Our computational techniques are based on the soft-sphere DEM simulations as developed by Cundall and Strack [34], Walton [35], and Luding [36–38]. The normal force between particles in contact is modeled by a Hookean spring as $f_n = -k_n \delta_n - \eta_n v_n$, where k_n, δ_n, η_n, and v_n are the normal stiffness, particle overlap, normal viscous damping coefficient, and relative velocity in the normal direction, respectively. Similarly, the tangential force is modeled as $f_t = -k_t \delta_t - \eta_t v_t$, where $k_t = 2k_n/7$, δ_t, $\eta_t = \eta_n/4$, and v_t are the tangential stiffness, relative displacement in tangential direction, tangential viscous damping coefficient, and relative velocity in tangential direction, respectively. We also introduce Coulomb's friction between the particles, where the tangential force f_t is switched to the sliding force $|f_s| = -\mu_p |f_n|$, μ_p being the particle friction coefficient when f_t exceeds the critical value, i.e. $|f_t| > \mu_p |f_n|$ (with $\mu_p = 0.01$) [38].

To study the effect of particle softness on the macroscopic behavior, we explore a range of normal contact stiffness k_n, from $10\ \mathrm{Nm}^{-1} \leqslant k_n \leqslant 10^4\ \mathrm{Nm}^{-1}$. When k_n is changed, k_t, η_n, and η_t are changed as well to ensure that the coefficients of restitution remain unchanged. While changing k_n, the time step for numerical integration δt is adjusted such that it much smaller compared the contact duration to ensure accurate dynamic integration [38].

2.2. Split-bottom ring shear cell

Figure 1 is a sketch of our numerical setup [39–42]. In this figure, the inner, split, and outer radii are given by R_i, R_s, and R_o, respectively, where the concentric cylinders rotate relative to each other at a rate Ω around the symmetry axis (the dot-dashed line). The ring shaped split at the bottom separates the moving and static parts of

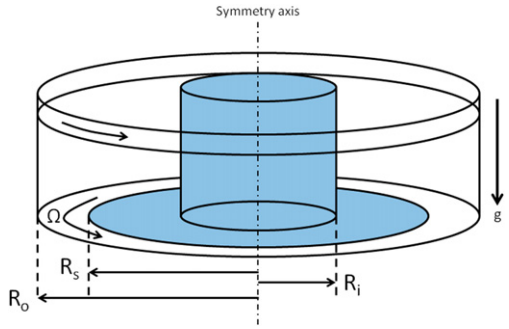

Figure 1. A sketch of our numerical setup consisting of a fixed inner part (light blue shade) and a rotating outer part (white). The white part of the base and the outer cylinder rotate with the same angular velocity, Ω, around the symmetry axis (dot-dashed line). The inner, split, and outer radii are given by $R_i = 8\langle a\rangle$, $R_s = 80\langle a\rangle$, and $R_o = 100\langle a\rangle$, respectively, where each radius is measured from the symmetry axis. The gravity, g, points downwards as shown by an arrow.

Table 1. Table showing the values of $\frac{\Omega}{2\pi}$ (units of s^{-1}), g (units of ms^{-2}) and particle stiffness k_n (units of Nm^{-1}) used in our simulations, and various time scales associated with the system (in units of s), as discussed in the main text. The values of $T_{\dot\gamma}$ and T_p are the average values reported at $z = 2\langle d\rangle$, $H/2$, $H - 2\langle d\rangle$ in the center of the shear band.

g	$\frac{\Omega}{2\pi}$	k_n	T_c ($\times 10^{-3}$)	T_η ($\times 10^{-2}$)	T_g ($\times 10^{-2}$)	$T_{\dot\gamma}$	T_p ($\times 10^{-3}$)
0.5	0.005	100	2	5.6	6.6	25, 20, 10	1.7, 2.5, 5
1	0.01	100	2	5.6	4.7	10.9, 7.8, 2.7	12.5, 15.3, 32
2	0.01	100	2	5.6	3.3	10.7, 7.5, 2.7	9, 11, 22
5	0.01	100	2	5.6	2.1	10.3, 7.4, 2.6	5.9, 7, 14.6
5	0.01	500	0.1	2.5	2.1	10.6, 7.5, 2.1	5.1, 7, 14.1
20	0.01	100	2	5.6	1.05	9.7, 7.0, 2.6	2.9, 3.8, 8
20	0.01	400	10	11.2	1.05	10, 7.1, 2.7	2.9, 3.6, 7.4
50	0.01	100	2	5.6	0.66	8.7, 6.6, 2.5	1.8, 2.2, 4
50	0.01	1000	0.66	18	0.66	10.1, 7.1, 2.6	1.9, 2.5, 7
10	0.01	100	2	5.6	1.5	9.9, 7.0, 2.6	4, 5.6, 24
10	0.01	1000	0.66	18	1.5	9.1, 8.1, 2.6	4, 5.6, 27
10	0.01	10000	0.2	0.56	1.5	10.7, 7.3, 2.8	4, 5.4, 31
10	0.1	100	2	5.6	1.5	1.1, 0.7, 0.23	4, 6, 9
10	0.5	100	2	5.6	1.5	0.2, 0.15, 0.05	4, 5, 10
10	1.0	100	2	5.6	1.5	0.1, 0.07, 0.02	4, 5, 20
10	2.0	100	2	5.6	1.5	0.02 0.03, 0.008	4, 6, 18

the system, where a part of the bottom and the outer cylinder rotate at the same rate. The system is filled with $N \approx 3.7 \times 10^4$ polydispersed spherical particles with density $\rho_p = 2000\ kgm^{-3} = 2\ gcm^{-3}$ up to height H.

The average size of particles is $\langle a\rangle = 1.1$ mm, and the width of the homogeneous size-distribution (with $a_{min}/a_{max} = 1/2$) is $1 - \mathcal{A} = 1 - \langle a\rangle^2/\langle a^2\rangle = 0.0357$. The cylindrical walls and the bottom are roughened by attaching some (about 3% of the total number) attached/glued particles [41, 43, 44].

When there is relative motion between inner and outer cylinders, a shear band initiates at the bottom from the split position R_s and propagates upwards and inwards, remaining far away from the cylindrical walls in most cases [40, 42]. The qualitative behavior is governed by the ratio H/R_s and three regimes can be observed as reported in [40, 42]. We choose $H \backsimeq 0.034$ m (for $g = 10\ ms^{-2}$ and $k_n = 100\ Nm^{-1}$)[1], such that azimuthal velocity profiles always have the error function shape. The shear band always reaches the free top surface and stays away from the walls, as reported in [40]. With increasing filling height (data reported in [45]), the shear band at the top surface gets wider and moves inwards, before stronger deviations from the error function are observed [42]. However, for none of our simulations we observed instabilities as recently reported by Moosave *et al* [46]. Our simulations indicate (data not shown) that the width decreases and the position moves less inwards with increasing k_n and g.

To study the bulk behavior in a broad pressure range, gravity is varied in the range $0.5\ ms^{-2} \leqslant g \leqslant 50\ ms^{-2}$. The details regarding rotation rate of the system are reported in table 1. The total simulation time is chosen such that the cylinder completes half a rotation in that time.

[1] The height varies slightly with gravity and particle softness.

2.3. Local averaging

One of the goals of current research in the granular community is to derive macroscopic continuum theory based on the given micro-mechanical properties [47–49]. In our cylindrical cell, we assume translational invariance in the azimuthal $\theta-$ direction. The averaging is thus performed over toroidal volumes over many snapshots in time, leading to generic fields $Q(r,\ z)$ as function of the radial and vertical positions. Here, the averaging is performed with spacings Δr and Δz around two particles diameter in radial and vertical directions (averaging procedure for two and three dimensions is discussed in detail in [43, 48] and hence not discussed further here). We tested our results for averaging with different spacings (two, three, and four particle diameters) and the results are found to be unaffected.

2.3.1. Macroscopic (tensorial) quantities

Here, we present general definitions of the averaged macroscopic quantities—including strain rate, stress, and fabric (structure) tensors.

The strain rate is calculated by averaging the velocity gradient of the particles over the cell with volume V and is given by

$$\dot{\epsilon}_{\alpha\beta}(\mathbf{r}) = \frac{1}{2}\sum_{i\in V}\left(\bigtriangledown_\beta \mathrm{v}^i_\alpha + \bigtriangledown_\alpha \mathrm{v}^i_\beta\right), \tag{1}$$

with particle i, velocity v^i, and Greek letters represent the cylindrical components, radial distance r, azimuthal angle θ, and height z, while $\bigtriangledown$ represents the gradient in cylindrical coordinate [43].

The stress tensor is given by

$$\sigma_{\alpha\beta}(\mathbf{r}) = \frac{1}{V}\left[\sum_{i\in V} m^i \delta \mathrm{v}^i_\alpha \delta \mathrm{v}^i_\beta - \sum_{c\in V} l^c_\alpha f^c_\beta\right], \tag{2}$$

with particle i, contact c, mass m^i, fluctuations velocity $\delta \mathrm{v}^i$, force f^c, and branch vector l^c. The first term is the sum of kinetic energy fluctuations, and the second term involves the dyadic product of the contact force with the contact-branch vector.

The quantity which describes the local configuration of a granular assembly is the fabric tensor [49, 50] and is given by

$$F_{\alpha\beta}(\mathbf{r}) = \frac{1}{V}\sum_{i\in V} V^i \sum_{c\in i} n^c_\alpha n^c_\beta, \tag{3}$$

where V^i represents the particle volume which lies inside the averaging volume V, n^c is the normal unit branch-vector pointing from the center of particle i to contact c.

2.3.2. Isotropic and deviatoric parts

Any given tensor $\boldsymbol{Q}$ can be uniquely decomposed into isotropic and deviatoric parts as

$$\boldsymbol{Q} = Q_V \boldsymbol{I} + \boldsymbol{Q_D} \tag{4}$$

with I being the identity matrix, $Q_V = \frac{1}{3}\,\mathrm{Tr}\,\boldsymbol{Q}$ and the traceless deviator $\boldsymbol{Q_D}$. The latter contains information about the eigensystem of $\boldsymbol{Q}$, that is identical to the eigensystem of $\boldsymbol{Q_D}$ itself.

Let us assume Q_1, Q_2, and Q_3 are the eigenvalues of $\boldsymbol{Q_D}$ sorted such that $Q_1 \geqslant Q_2 \geqslant Q_3$. Based on the normalization, we use the following definition to quantify the anisotropy of any tensor $\boldsymbol{Q_D}$ using a single scalar quantity:

$$Q_{\mathrm{dev}} = \sqrt{\frac{\left(Q_1 - Q_2\right)^2 + \left(Q_2 - Q_3\right)^2 + \left(Q_3 - Q_1\right)^2}{6}}, \tag{5}$$

the deviators $\dot{\epsilon}_{\mathrm{dev}}$, σ_{dev}, and F_{dev} refer to strain rate $\dot{\epsilon}_{\alpha\beta}$, stress $\sigma_{\alpha\beta}$, and fabric $F_{\alpha\beta}$, respectively. While $Q_{\mathrm{dev}} = |Q_1 - Q_3|$ for plane strain simulations ($Q_2 = 0$), alternative definitions of Q_{dev} are reported in [51] using other (Frobenius) normalization better suited for the elastic regime.

$\dot{\gamma} = \dot{\epsilon}_{\mathrm{dev}}$ quantifies the local strain-rate magnitude, which is very close to the form defined in cylindrical coordinates [52] as tested in [43]. The pressure p is the isotropic hydrostatic stress, while $\tau = \sigma_{\mathrm{dev}}$ quantifies objectively the shear stress. The deviatoric stress ratio, $\mu = \tau/p$, is the effective macroscopic friction. The volumetric fabric $3F_{\mathrm{v}}$ represents the contact number density, while the deviatoric fabric F_{dev} quantifies the anisotropy of the contact network (as studied in detail in [53]).

2.4. Time scales

To characterize the dynamics of the system, we look at different time scales. At first, we define two microscopic time scales related to the contact duration and the viscous damping coefficient between two particles in contact, respectively, as

$$T_k = \sqrt{\frac{\langle m \rangle}{k_n}}, \; T_\eta = \frac{\langle m \rangle}{\eta_n}, \tag{6}$$

where $\langle m \rangle$ is the mass of a particle with mean diameter. T_k and T_η can be related to contact duration $T_c = \frac{\pi}{\sqrt{\frac{1}{T_k^2} - \frac{1}{T_\eta^2}}}$ [2]. Next, two time scales associated with external forces, i.e., the gravity and external rotation rate, can be introduced as

$$T_g = \sqrt{\frac{\langle d \rangle}{g}}, \; T_\Omega = \frac{2\pi}{\Omega}, \tag{7}$$

respectively, where T_g is the time taken by a particle with zero initial velocity to fall a distance $\langle d \rangle/2$, and T_Ω is the time taken by the system to complete a rotation.

The time scales, (6) and (7), are functions of material constants and applied external forces, hence, are constants throughout the system. In this sense, the time scales, T_c, T_η, T_g, and T_Ω, are *global*. On the other hand, two local time scales related to the local shear rate $\dot{\gamma}$ and pressure p, as introduced in [6, 55], are:

$$T_{\dot{\gamma}} = \frac{1}{\dot{\gamma}}, \; T_p = \langle d \rangle \sqrt{\frac{\rho}{p}}, \tag{8}$$

with ρ being the bulk density.

As shown in the following sections, the spatial distributions of pressure and shear rate are inhomogeneous due to gravity and shear localization. Therefore, in contrast to the global time scales, $T_{\dot{\gamma}}$ and T_p are *local* field variables that depend on spatial position.

The time scales can be combined to formulate dimensionless numbers that give indications of dominance of one time scale over the other. For example, the inertial number, as introduced in [7, 8, 55],

$$I \equiv T_p / T_{\dot{\gamma}} = \dot{\gamma} \langle d \rangle / \sqrt{p/\rho}, \tag{9}$$

provides an estimate of the local rapidity of the flow. For $I \ll 1$, the flow is *quasistatic*, where particles interact via enduring contacts and inertial effects are negligible. For $I \sim 1$, the flow is in the *dense inertial regime*, and for $I \gg 1$, the flow is in the rapid, collisional gas-like state[3]. Other expressions have been introduced by various authors, such as the Savage or Coulomb number $\dot{\gamma}^2 \langle d \rangle^2 \rho / p$, that are simply the square of the inertial number I [56].

A dimensionless parameter, the *global compressibility*, can be introduced as the ratio between T_k and T_g:

$$\kappa_g \equiv \frac{T_k}{T_g} = \sqrt{\frac{\langle m \rangle g}{k_n \langle d \rangle}}, \tag{10}$$

providing a global measure of compressibility of the bulk material. A high κ_g signifies that the bulk material is compressible, which comes from either very high confinement by strong gravity or from low contact stiffness at particle level. On the other hand, when κ_g is small, the average overlap is very small compared to the particle diameter, which means that the bulk material is closer to the rigid limit. A similar dimensionless parameter can be introduced as

$$\kappa_p \equiv \frac{T_k}{T_p} = \sqrt{\frac{p \langle d \rangle}{k_n}}, \tag{11}$$

which estimates the compressibility of the material at the local scale[4].

Table 1 shows typical values of time scales in our simulations, and table 2 reports various dimensionless numbers. We observe that for flows with a rotation rate $\Omega/2\pi = 0.01$ s^{-1} and gravity $g \geqslant 1$ ms^{-2}, the inertial number I is well below one for all values of k_n. For lower values of gravity $g = 0.5$ ms^{-2}, the rotation rate is chosen to be $\Omega/2\pi = 0.005$ s^{-1}, such that I stays in the same range. From this table we infer that the system can

[2] In case of a Hertzian contact model the time scale related to contact duration will be $T_k = Cp^{-1/6}$, where p is the compression, and C is a material parameter constant. For details, please refer to [54].

[3] A variant of inertial number $I_k = \dot{\gamma} \langle d \rangle / \sqrt{p_{kin}/\rho}$ can be defined by using only the kinetic pressure instead of the total pressure (See (2)).

[4] In case of a Hertzian contact model, it would be pressure dependent as $\kappa_p \propto p^{1/3}$, where the constant of proportionality is a material parameter constant.

Table 2. Table showing the values of g (units of ms^{-2}) and particle stiffness k_n (units of Nm^{-1}) used in our simulations, and various dimensionless numbers, as discussed in the main text. The average values of I are reported at $z = 2\langle d\rangle$, $H/2$, $H - 2\langle d\rangle$ in the center of the shear band.

g	$\frac{\Omega}{2\pi}$	k_n	I	κ_g^2
0.5	0.005	100	$(7, 12, 50)\times10^{-3}$	2×10^{-5}
1	0.01	100	$(1.3, 2, 4)\times10^{-3}$	5×10^{-4}
2	0.01	100	$(0.75, 2, 1.4)\times10^{-3}$	3.4×10^{-3}
5	0.01	100	$(2, 0.7, 0.9)\times10^{-3}$	1×10^{-3}
5	0.01	500	$(2.5, 0.8, 1.4)\times10^{-3}$	2×10^{-4}
20	0.01	100	$(1, 0.5, 0.9)\times10^{-3}$	1×10^{-3}
20	0.01	400	$(2, 4, 7)\times10^{-4}$	1×10^{-4}
50	0.01	100	$(8, 3.4, 7.2)\times10^{-5}$	2.5×10^{-3}
50	0.01	1000	$(5, 3, 6)\times10^{-5}$	2.5×10^{-4}
10	0.01	100	$(1.1, 0.6, 1.5)\times10^{-3}$	5×10^{-4}
10	0.01	1000	$(1.4, 0.5, 1.6)\times10^{-3}$	5×10^{-5}
10	0.01	10000	$(1.2, 0.6, 0.9)\times10^{-3}$	5×10^{-6}
10	0.1	100	$(1.5, 0.6, 0.9)\times10^{-2}$	5×10^{-4}
10	0.5	100	$(7.5, 2.6, 6)\times10^{-2}$	5×10^{-4}
10	1.0	100	$(1.5, 0.5, 10.2)\times10^{-1}$	5×10^{-4}
10	2.0	100	0.3, 0.16, 1.51	5×10^{-4}

be safely assumed to be in the rate-independent quasistatic state for a wide range of g and k_n. However, we observe that with an increase in rate of rotation $\Omega/2\pi$, I begins to increase and the flow behavior enters into the rate-dependent inertial regime.

3. Quasistatic rheology

3.1. Critical state

Shearing of a granular system leads to volume dilation and build-up of shear stress and anisotropy in fabric (quantified by deviatoric fabric). Since we are interested in the steady-state flow properties, we need to know what is the minimum time (or equivalent strain) required to reach the steady-state flow regime.

We define $\varphi = \Omega\Delta t$, an angle through which the system rotates (where Δt is the simulation time) as the shear control parameter. In general, the time required for stabilization depends on the variable considered [9]. In the following, we check the relaxation of various quantities (both locally and globally averaged) towards the steady state. As we expect this relaxation to be slower for small Ω (due to small dissipation), we study the relaxation behavior for $\Omega/2\pi = 0.01$ s^{-1} that is the smallest Ω in our simulations.

At first, we analyze the global quantities (averaged over the whole system) like the kinetic energy and average number of contacts. Both quantities saturate very fast ($\varphi \sim 5°$). Next, we analyze the relaxation of local quantities, specifically the local velocity profiles. We conclude that $\varphi \sim 30°$ is the time required to form a stable shear band, which is in agreement with Ries *et al* [31] and Wortel *et al* [57]. Consequently, we perform the local averaging over almost 600 snapshots distributed over $\varphi \geqslant 30°$.

The consistency of the local averaged quantities also depends on the accumulated local shear strain during the averaging time. We concentrate our interest in the region where the system can be considered in a critical state. The critical state is a unique steady state reached after long shear, where material deforms with applied strain without any further change in normal stress, shear stress, and volume fraction, and the system forgets its preparation history [58]. In accordance with the previous experimental and numerical results in the same setup [43, 59], we chose shear strain $\gamma = \dot{\gamma} t_{av} \geqslant 1$ to be an estimate for the critical state (t_{av} is the averaging time). In other words, for $\dot{\gamma} \geqslant \frac{1}{t_{av}} \equiv \dot{\gamma}_c$, the part of the system can be assumed to be in critical state.

Figure 2(a) shows the local shear stress $\tau(r,\ h)$ plotted against the local pressure $p(r,\ h)$. Since the system is non-homogeneous in nature, for a given pressure we observe a wide range of local strain rate $\dot{\gamma}$ and we find that τ is higher for larger $\dot{\gamma}$. However for $\dot{\gamma} > \dot{\gamma}_c$ (with $\dot{\gamma}_c \approx 0.08$ s^{-1}), τ becomes almost independent of the local strain. This means that τ/p is almost constant for all data points with strain rate $\dot{\gamma} > \dot{\gamma}_c$.

In the same setup, Ries *et al* [31] and Szabó *et al* [59] also found that after long enough shear, the material inside the shear band reaches the critical state, and characterized this condition by the local accumulated strain $\gamma \geqslant 1$. Our previous works [43, 60] also showed that for rotation rate $\Omega/2\pi = 0.01$ s^{-1}, $\dot{\gamma}_c \approx 0.1$ s^{-1} is the shear rate above which the shear band is well established. Since we are interested in the flow behavior of the material, as default in the rest of the paper we focus only on the data well inside the shear band with local strain rate,

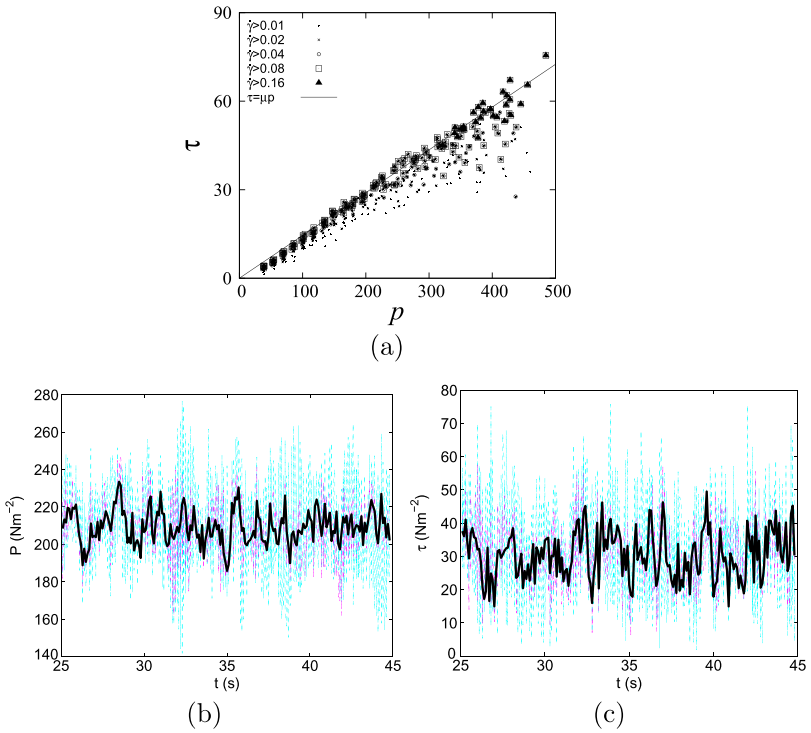

Figure 2. (a) The local shear stress, $\tau\,(r,\,h)$, plotted against the local pressure, $p\,(r,\,h)$, for different values of the local shear rate, $\dot{\gamma}\,(r,\,h)$ as given in the legend (in units of s^{-1}). (b) Pressure p, and (c) shear stress τ plotted against time t for the spatial position $r = 0.08$ m (center of shear band) and $h = 0.022$ m. Cyan, magenta, and black colors represent the results obtained by averaging using cell size of 1, 1.5, and 2 particle diameters, respectively, in the r- and z-direction, with a quarter ring in the azimuthal direction. The data reported here are from a simulation with $g = 10$ ms^{-2} and $\Omega/2\pi = 0.01$ s^{-1}.

$$\dot{\gamma}\,(r,\,h) > \dot{\gamma}_c\,(\Omega) \equiv \frac{10\Omega}{2\pi}, \tag{12}$$

unless specified otherwise.

Figures 2(b) and (c) show the steady-state pressure and shear stress plotted against time, respectively, for different averaging spacings in r and z (1, 1.5, and 2 particle diameters). For the sake of clarity, data for only one spatial point (center of shear band at mid-height) are plotted. We observe that the size of averaging spacing does not affect the mean (averaged) results, only that the standard deviation. The results from the smallest cell size, i.e., one particle diameter, show the maximum scatter or variation of data; the pressure varies only relatively little (8%), whereas the shear stress varies a lot more (35%). (In this study we do not attempt to unravel the contributions that are due to statistical fluctuations and the real time-evolution of the system, i.e., increase (semi-elastic) and decrease (plastic rearrangement) of stresses, on short time scales.) In the rest of the paper, the averaging of the data is performed over cell sizes of two particle diameters, unless specified otherwise.

3.2. Effective friction coefficient

We will now turn our attention towards the effect of pressure and softness on the effective macroscopic friction τ/p in the quasistatic state. In previous studies, it has been assumed to be independent of both the particle stiffness and pressure [6, 7]. However, particles used in these cases were extremely rigid. Few studies were performed systematically investigating the flow behavior in the low pressure/gravity regime [18–23].

Figures 3(a) and (b) show shear stress-pressure curves for different values of normal stiffness k_n and external gravity g, respectively. In these plots, for the sake of clarity, both shear stress and pressure are plotted only at the center position R_c of the shear band (R_c being the position at which both τ and the local shear rate are maximal). For a better comparison, both shear stress and pressure are normalized with the maximum pressure p_{max} reached in the simulation with particular k_n and g (so that both abscissa and ordinates are of the same order)[5]. We observe that both softness of the particles (interpreted as opposite of contact stiffness) and gravity drastically affect the shear stress. Moreover, they act in the same direction as τ decreases with increase in either particle softness or external gravity. We also see that for the most soft particles or the higher gravity data, the relation between τ and p is non-linear.

[5] The error-bars show the standard deviation of the data in time.

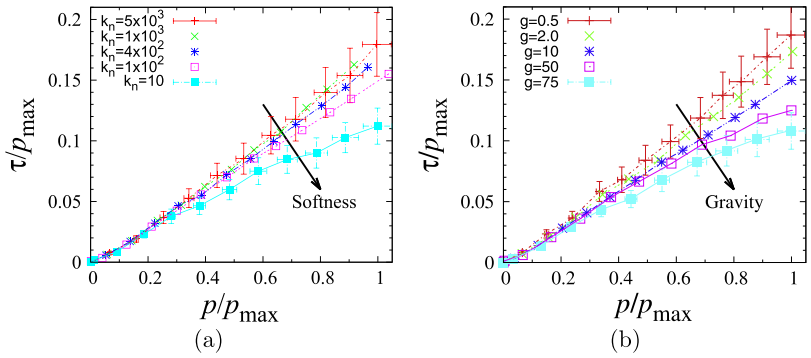

Figure 3. (Left) Shear stress plotted against the local pressure for different values of the softness (interpreted as opposite to the normal stiffness) as given in the legend in units of Nm^{-1}. Here, the gravity is fixed to $g = 10\ \mathrm{ms}^{-2}$. (Right) The local shear stress plotted against the local pressure for different values of the gravity as given in the legend in units of ms^{-2}. Here, the normal stiffness is fixed to $k_n = 100\ \mathrm{Nm}^{-1}$. Both $\tau(r, h)$ and $p(r, h)$ are scaled by the maximum pressure $p_{\max}(r, h)$, respectively.

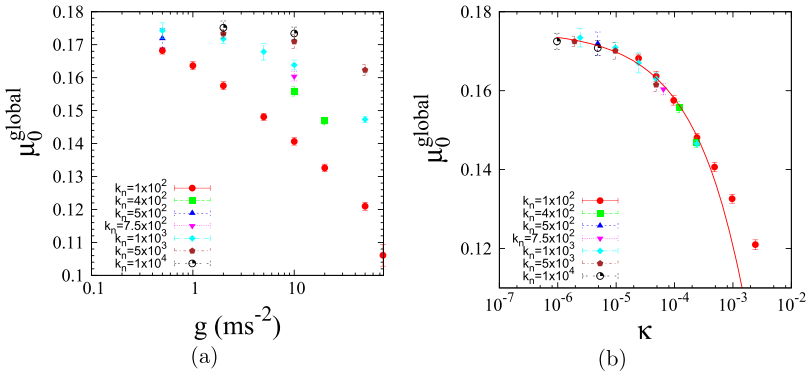

Figure 4. The global friction coefficient, μ_0^{global}, plotted against (left) gravity g, and (right) the global compressibility, $\kappa = \langle m \rangle g/(k_n \langle d \rangle)$, on a log-linear scale for different values of the normal stiffness as shown in the legend. The solid line represents (14).

3.2.1. Linear approximation

To understand the dependence of the effective macroscopic coefficient in a quasistatic state on softness and gravity (pressure), we estimate it as the slope of a linear fitting function for the shear stress against pressure in the same fashion as the Mohr-Coulomb failure criterion, i.e.,

$$\tau(h) \simeq \mu_0^{\mathrm{global}} p(h), \tag{13}$$

where μ_0^{global} is the *global friction coefficient* for a given system.

Figure 4(a) displays the global friction coefficient μ_0^{global} plotted against gravity g for different values of the normal stiffness k_n, as given in the legend. We observe that μ_0^{global} decreases with increasing gravity, while it increases with increasing k_n. It is important to mention that μ_0^{global} is obtained by fitting the data to (13), i.e., it is not the average of $\frac{\tau(r,h)}{p(r,h)}$ for different heights in the system. As we observe that the $\tau - p$ relation becomes non-linear with increase in gravity or softness, as a first attempt we fit the data to a linear Mohr–Coulomb failure criterion (13). For the fitting, all the data in the range $0 \leqslant p \leqslant p_{\max}$ are chosen. The error bars represent the error in fitting the data, which increases with increase in softness/gravity. Figure 4(b) shows the global friction coefficient with different values of the normal stiffness k_n and gravity g, where all results of μ_0^{global} are collapsed, if we plot them against $\kappa = \kappa_g^2$ (κ_g is given in (10)).

In figure 4(b), the solid line is given by

$$\mu_0^{\mathrm{global}} = \mu_r^{\mathrm{global}} - \left(\frac{\kappa}{\kappa_0}\right)^{\alpha}, \tag{14}$$

where $\mu_r^{\mathrm{global}} = 0.17 \pm 0.01$ is the global friction coefficient in the rigid particle limit and the exponent and characteristic global compressibility are given by $\alpha \simeq 0.5$ and $\kappa_0 \simeq 2.01$, respectively.

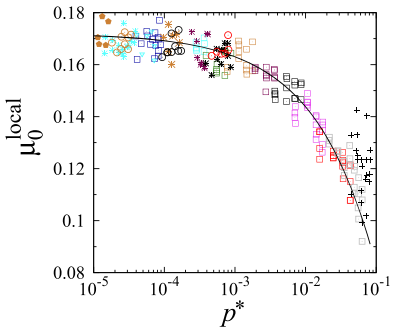

Figure 5. The local effective friction coefficient, $\mu_0^{\text{local}}(p^\star)$, plotted against the local dimensionless pressure, $p^\star$, on a log-linear scale. Different symbols represent different values of κ as given in the legend of figure 6, while the solid line represents (17). Local data are shown for $\dot{\gamma} > \dot{\gamma}_c = 0.1\ \text{s}^{-1}$.

Previous microgravity parabolic flight and centrifuge experiments [18, 20–24] showed a similar decreasing trend of the effective macroscopic friction coefficient on gravity. Some authors [20, 23] attributed this dependence to the fact that at low gravity, the body forces become weak and the electrostatic cohesive forces begin to dominate. Klein *et al* [20] also argued that a load-dependent interparticle friction coefficient might be responsible for this behavior. However, no cohesive force or load-dependent friction was implemented in any of the DEM simulation data presented here. Hence, we claim that there should be an additional mechanism responsible for this interesting behavior. In order to gain a better understanding of the nonlinear behavior, in the following, we study the system locally.

3.2.2. Local dimensionless pressure

Since our system is non-homogeneous in both stress and strain-rate fields, a local description of the system is highly desirable. In the shear stress-pressure ($\tau - p$) curves for different softness and gravity (figure 3), the dependence of shear stress on pressure slightly 'bends' with increasing softness and gravity, i.e., the friction coefficient develops a dependence on the pressure:

$$\tau(r, h) = \mu_0^{\text{local}}\left(p, k_n\right) p(r, h), \tag{15}$$

where $\mu_0^{\text{local}}(p, k_n) = \tau(r, h)/p(r, h)$ is the *local effective friction coefficient* which depends on both pressure and contact stiffness.

Figure 5 shows the local effective friction coefficient for different values of the normal stiffness and gravity, where all results of $\mu_0^{\text{local}}(p, k_n)$ collapse if we introduce the *local dimensionless pressure*,

$$p^\star \equiv \kappa_p^2 = \left(\frac{T_k}{T_p}\right)^2 = \frac{p\langle d\rangle}{k_n}, \tag{16}$$

defined as square of the ratio between two time scales, T_k and T_p, in section 2.4 [6]. $p^\star$ can also be interpreted as non-dimensional average overlap (scaled with mean particle diameter). In this figure, we scanned through a wide range of $p^\star$ by systematically varying g and k_n. We observe that for $p^\star < 5 \times 10^{-4}$, $\mu_0^{\text{local}}(p^\star)$ is almost constant, while for higher values, $\mu_0^{\text{local}}(p^\star)$ decreases with $p^\star$ up to $p^\star \approx 0.1$.

This dependence can be written in the form,

$$\mu_0^{\text{local}}\left(p^\star\right) = \mu_{\text{r}}^{\text{local}} - \left(\frac{p^\star}{p_\sigma^\star}\right)^{\beta_1}, \tag{17}$$

where $\mu_{\text{r}}^{\text{local}} = 0.172 \pm 0.01$ is the value of effective friction in the rigid limit, which is in fair agreement with contact dynamics shear simulations for the same particle friction coefficient [62]. The exponent is found to be $\beta_1 \approx 0.5 \pm 0.04$ and the characteristic local dimensionless pressure is $p_\sigma^\star = 10.1 \pm 0.2$. As one extreme of $p^\star$, for $p^\star = 0.1$ the average overlap is order of 10% relative to the mean particle diameter, i.e., the *soft particle limit*. The upper bound of $\mu_0^{\text{local}}(p^\star)$ is the low compression case, i.e., *the rigid limit*, where the average overlap is much smaller (10^{-4}) compared to the particle diameter. $\mu_0^{\text{local}}(p^\star)$ in the rigid limit is almost double as large compared to the soft particle limit for $p^\star \approx 0.1$.

[6] The non-dimensional form of pressure will be different in case of a Hertzian system [61].

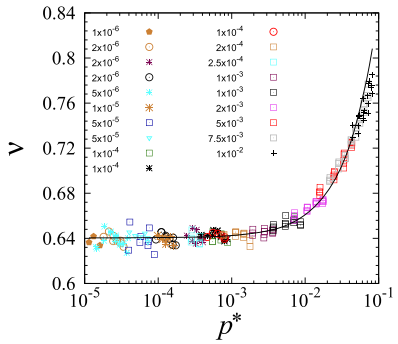

Figure 6. The local volume fraction, $\nu\,(r,\,h)$, in the system plotted against the local dimensionless pressure, $p^{\star}$, on a log-linear scale. Different symbols represent different values of κ as given in the legend. The solid line represents (18). Local data are shown for $\dot{\gamma} > \dot{\gamma}_c = 0.1\ \mathrm{s}^{-1}$.

3.3. Local volume fraction

In figure 6, the local volume fraction $\nu\,(r,\,h)$ is plotted against the local dimensionless pressure, $p^{\star}$. Because of slow quasistatic flows, no strong dilation is observed, i.e., no strong dependence of ν on local shear rate. The packing is rather loose for lower $p^{\star}$ and tends to a critical value $\nu_c = 0.642 \pm 0.002$, in agreement with [63]. The data can be fitted well by the functional form

$$\nu = \nu_{\mathrm{c}} + \frac{p^{\star}}{p^{\star}_{\nu}}, \tag{18}$$

with $p^{\star}_{\nu} = 0.48 \pm 0.02$ ($p^{\star}_{\nu}$ can be further expressed in terms of volumetric fabric as reported in [64]). Interestingly, no significant difference in volume fraction ν is observed for $p^{\star} < 10^{-3}$, while for $p^{\star} > 10^{-3}$ within the fluctuations, ν increases almost linearly with $p^{\star}$ (the curvature is due to the logarithmic $p^{\star}$ axis). The relation between ν and $p^{\star}$ is well established in the case of static packings [64, 65]. Here we show that the same relation holds for a slow granular flow, involving considerable small but finite strain rates.

3.4. Local structure

Shearing of a granular assembly always leads to the buildup of contact anisotropy in the system [66–68]. To study this property we analyze the deviatoric fabric as defined in (3) and use (5) to quantify anisotropy of the contact network.

3.4.1. Local anisotropy

Figure 7 displays the local deviatoric fabric, $F_{\mathrm{dev}}\,(r,\,h)$, plotted against the local dimensionless pressure $p^{\star}$, where $F_{\mathrm{dev}}\,(r,\,h)$ for different values of the particle stiffness and gravity is found to collapse on a unique curve (solid line). This dependence can be written in a similar fashion as (17),

$$F_{\mathrm{dev}}\left(p^{\star}\right) = F^{r}_{\mathrm{dev}} - \left(\frac{p^{\star}}{p^{\star}_{F}}\right)^{\beta_2}, \tag{19}$$

where F^{r}_{dev} is the anisotropy of contact network in the rigid limit, the exponent is found to be $\beta_2 \approx 0.5 \pm 0.03$, and $p^{\star}_{F} \approx 26.3 \pm 0.6$. The decrease in F_{dev} with increasing $p^{\star}$ can be explained in terms of the increasing volume fraction $\nu\,(r,\,h)$ with increase in $p^{\star}$. When the packing becomes denser, particles have less free space to (re) arrange. Hence they cannot align along the preferential direction, thus anisotropy in response to the local shear is found to decrease with increase in $p^{\star}$.

In figures 5 and 7, we observe that the local effective friction and the local contact anisotropy show a similar trend in the quasistatic state ($\beta_1 \backsimeq \beta_2$). In figure 8, we plot $\mu_0^{\mathrm{local}}\,(p^{\star})$ against $F_{\mathrm{dev}}\,(p^{\star})$ for different values of κ, where a linear correlation can be inferred as,

$$\mu_0^{\mathrm{local}}\left(p^{\star}\right) = \mu_{\mathrm{iso}} + bF_{\mathrm{dev}}\left(p^{\star}\right), \tag{20}$$

where $\mu_{\mathrm{iso}} = 0.01 \pm 0.01\,(\approx 0)$ is the effective friction coefficient in the (extrapolated) limit of the *isotropic* contact network ($F_{\mathrm{dev}} = 0$) and $b = 1.38 \pm 0.02$ is a constant of proportionality. This clearly shows that in the critical state, the shear resistance accompanies the anisotropy in the contact network. The linear relation can be a consequence of the linear contact model, the relation might be different in case of a Hertzian contact model. It is

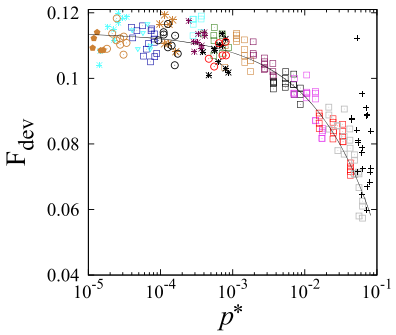

Figure 7. The local deviatoric fabric, $F_{\rm dev}\,(r,\ h)$, plotted against the local dimensionless pressure, $p^{\star}$, on a log-linear scale. Different symbols represent different values of κ as given in the legend of figure 6. The solid line represents the corresponding fit to (19). Local data are shown for $\dot{\gamma} > \dot{\gamma}_c = 0.1\ \mathrm{s}^{-1}$.

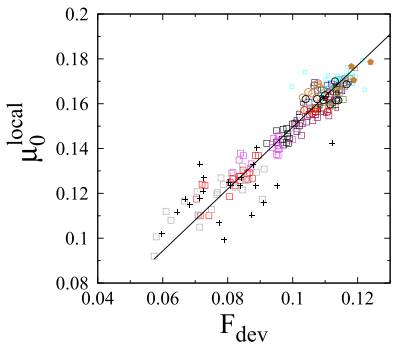

Figure 8. The local friction coefficient, $\mu_0^{\rm local}\,(p^{\star})$, plotted against the local deviatoric fabric, $F_{\rm dev}\,(r,\ h)$, for different values of κ. Different symbols represent different values of κ as given in the legend of figure 6. The solid line represents the corresponding fit to (20). Local data are shown for $\dot{\gamma} > \dot{\gamma}_c = 0.1\ \mathrm{s}^{-1}$.

worthwhile to mention that no information about such a relation in the transient regime (that leads to the critical state) can be inferred from our analysis. This correlation explains the increase in the effective friction coefficient with decreasing gravity/softness (as observed in figure 4(a)). With increase in gravity/softness the system becomes denser, hence the free space available to particles decreases. Hence $F_{\rm dev}$ decreases leading to a decrease in $\mu_0^{\rm local}$.

3.4.2. Shape factor

In this section, we compare the shape factor (Q_2/Q_1) for stress and fabric tensors, where Q_2, and Q_1 are the eigenvalues of the deviatoric tensors as defined in section 2.3.2. Due to geometry and symmetry, the state of strain in the shear band is plain strain, i.e., $\dot{\epsilon_2}/\dot{\epsilon_1} = 0$. We study the states of stress and fabric to understand the response of the granular flow to plain strain. We focus on the shape factor to quantify the ratio between the neutral eigenvalue (orthogonal to the shear plane) eigenvalue, to the maximum eigenvalue.

In figure 9(a), we plot the shape factor for the stress tensor. Different symbols represent different values of compressibility κ as given in the legend of figure 6, while black circles show the data in the center of shear bands for these simulations. We observe that the shape factor is highly fluctuating for the two extremes of $p^{\star}$, while in the range $10^{-4} < p^{\star} < 10^{-2}$, it is significantly below zero. This implies that the stress in the shear plane is higher as compared to the axial stress along the neutral direction orthogonal to the shear plane. The sign means that this axial stress is reduced perpendicular -1 and enhanced $+1/2$ within the shear plane [49]. The dashed line is the data from [49], where authors studied the flow behavior on an inclined plane. We observe that the sign for both the cases is negative, while the magnitude is different, which might be due to the difference in interparticle friction. In figure 9(b), the shape factor of the fabric tensor fluctuates (strongly) around zero. It is important to mention that the fluctuations in the data are from a single simulation.

These two observations suggest that fabric and stress tensors behave differently even though they are proportional in magnitude (norm), as shown in figure 8. The fabric tensor is in a planar state like the strain-rate tensor, whereas the induced stress state is triaxial, as expected for a solid-like material [49]. F_2/F_1 tends to positive

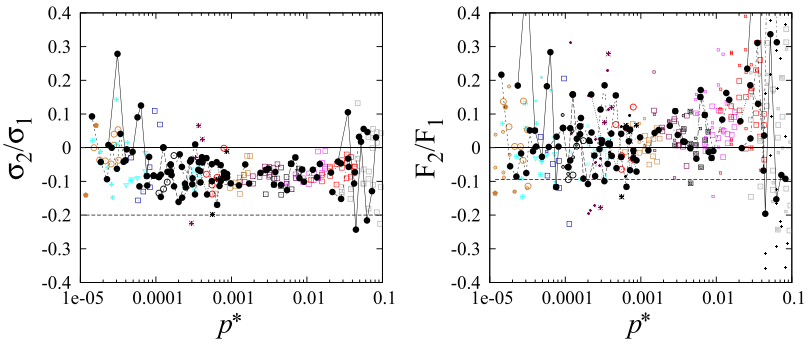

Figure 9. Shape factor for (left) stress, and (right) fabric plotted against local dimensionless pressure p^*. Different symbols represent different values of κ as given in the legend of figure 6. Black circles represent the data in the center of the shear band, other data are shown for $\dot{\gamma} > \dot{\gamma}_c = 0.1\ \mathrm{s}^{-1}$. Solid line represents zero, while dashed line is the prediction from [49].

values for larger p^*, further establishing the difference between structure and stress tensors. However, in order to have a clear picture for the fabric tensor, the strong and weak subnetworks should be studied separately, since only the strong subnetwork carries almost all of the fabric anisotropy [53, 69]. Along with a non-zero σ_2 eigenvalue we do expect other aspects to show up, like the non-collinearity of the stress/strain/fabric eigensystems, related to induced anisotropy. Nevertheless, these features cannot be investigated further here, due to the high fluctuations in the data.

As discussed in section 3.1 the cutoff shear rate $\dot{\gamma}_c$ can depend on the simulation time or the averaging time. In this section, we focused on the data only inside the shear band, which are in the critical state and have forgotten their initial configuration due to large strain. However, the velocity gradients in the setup are smooth, which implies that part of the system outside the shear band is also flowing, albeit slowly. If the simulation runs longer (and hence longer averaging time can be used), the cutoff can be lowered. Eventually, if the simulation would run infinitely long, no cutoff on the local strain rate is needed. If we reduce the cutoff on the local strain rate (see next section), by setting $\dot{\gamma}_c\ (\Omega) \equiv \frac{\Omega}{2\pi}$, we observe much wider variation of data for the local effective friction coefficient, the deviatoric fabric and the volume fraction. However, the qualitative picture (trend) remains unaffected for all measured quantities. However, the shape factors are not strongly influenced within a change in $\dot{\gamma}_c$, within nearly an order of magnitude. Only for very small $\dot{\gamma}$ deviations occur as presented next for faster and slower shear.

4. Combined rheology towards inertial regime

The previous section showed that in the quasistatic state the friction coefficient and deviatoric fabric are strongly correlated in the critical state, though their shape factors are found to be considerably different. Motivated by this, we check if this correlation also works in the rate-dependent inertial regime. To test the correlation, both lower and higher inertial number data are generated by varying the external rotation rate Ω for a fixed gravity $g = 10\ \mathrm{ms}^{-2}$ and contact stiffness $k_n = 100\ \mathrm{Nm}^{-1}$. In the following, we will explore the evolution of the local macroscopic friction coefficient μ and deviatoric fabric with the inertial number I and merge it with the dependence of both μ and deviatoric fabric on p^*, to propose a combined rheological law. As explained in the previous section and section 3.1, the cutoff shear rate for an established critical state also depends on the time interval for data procurement and the averaging time window. In this section, the total simulation and averaging times are increased. Hence, the cutoff on local strain rate is set to $\dot{\gamma}_c\ (\Omega) \equiv \frac{\Omega}{2\pi}$ so as to capture the maximum data (in the *critical state*) and present a unique local rheology law outside and inside the shear band.

4.1. Friction law

The local effective friction coefficient $\mu = \frac{\tau(r,h)}{p(r,h)}$ is plotted against inertial number I in figure 10. Different symbols show data from different rates of rotation as given in the legend; the black solid circles represent the data in the center of the shear band. The solid black line shows the friction law, as proposed in [7]:

$$\mu\left(I, p^\star\right) = \mu_0^{\mathrm{local}}\left(p^\star\right) + \frac{\mu_2^{\mathrm{local}}\left(p^\star\right) - \mu_0^{\mathrm{local}}\left(p^\star\right)}{1 + I_0^\sigma / I}, \tag{21}$$

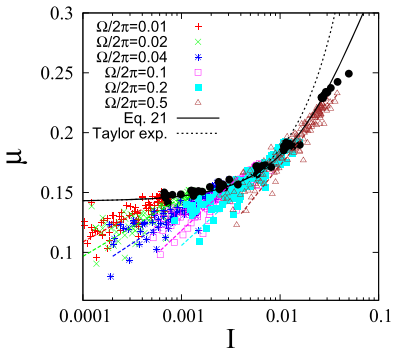

Figure 10. The local effective friction coefficient plotted against the inertial number I for results from simulations with different rates of rotation. The solid black line represents (21), with $\mu_0^{\text{local}} = 0.14$, $\mu_2^{\text{local}} = 0.3$, and $I_0^{\sigma} = 0.026$. The dotted line shows the Taylor expansion of (21). Different symbols represent different rates of rotation as given in the legend, lines with the same color represent the solution of (22). Black circles represent the data in the center of the shear band, other data are shown for $\dot{\gamma} > \dot{\gamma}_c = 0.01$ s^{-1}.

with $\mu_0^{\text{local}}(p^\star)$, a term that involves softness correction, as given in (17). We observe that data from a simulation using a single gravity ($g = 10$ ms^{-2}) and contact stiffness ($k_n = 100$ Nm^{-1}) does not give a wide variation in μ and $\mu_0^{\text{local}} = 0.14$, $\mu_2^{\text{local}} = 0.5$, and $I_0^{\sigma} = 0.1$ fit well the data. A Taylor expansion (in the range $I < I_0^{\sigma}$) for the preceding equation is $\mu(I) \cong \mu_0^{\text{local}} + (\mu_2^{\text{local}} - \mu_0^{\text{local}})\frac{I}{I_0^{\sigma}}$, which is similar to the linear frictional law proposed in [6, 55]. Two different trends emerge, i.e., the shear band center data can be very well fitted by (21) and for $I \geqslant 0.01$ data collapse on a unique curve. On the other hand, for lower values of I, deviations from this relation are observed, depending on the external rotation rate. The friction coefficient in slow flows (steady state) becomes smaller than μ_0^{local}, i.e., in our system the granular material is able to flow below μ_0^{local}. The deviation of our data from the main law (21) is consistent with observations in [9, 10], where this deviation is explained based on the heterogeneity in the stress field (arising due to strain rate). In our system, we have gradients in stress arising due to gradients in both strain rate and pressure.

In order to quantify the deviation from (21), we fit the data with:

$$\mu\left(I < I^\star, p^\star\right) = \mu_0^{\text{local}}\left(p^\star\right)\left[1 - \alpha \ln\left(I/I^\star\right)\right], \tag{22}$$

where α is a constant and $I^\star$ is the characteristic inertial number when $\mu \cong \mu_0^{\text{local}}$. This relation is inspired by the relation proposed in [9] for two-dimensional (2D) ring shear cell setup. As the relation was initially derived for a 2D setup with constant pressure, we fit it to our data at three different heights (i.e., constant pressure), close to top, at mid-height, and close to bottom. In figure 10, different colored dashed lines represent this fit at the mid-height of the system for each value of rotation rate explored. We observe that the prediction is in close agreement with the data, even though our system has different dimensions and boundary conditions. Data and corresponding fits for different heights (pressures) are reported in appendix A. We find that both α and $I^\star$ do not depend on pressure.

4.2. Fabric anisotropy

In order to look for the connection between anisotropic fabric and effective friction coefficient in the inertial regime, here we explore the dependence of F_{dev} on I. In figure 11, we plot the local F_{dev} as obtained by simulations with different rates of rotation against I. We observe that like μ, F_{dev} varies strongly against I and its dependence on I can be represented as:

$$F_{\text{dev}}\left(I, p^\star\right) = F_{\text{dev}}^0\left(p^\star\right) + \frac{F_{\text{dev}}^{(2)}\left(p^\star\right) - F_{\text{dev}}^0\left(p^\star\right)}{1 + I_0^F/I}, \tag{23}$$

with $F_{\text{dev}}^0(p^\star)$ being the fabric anisotropy in the quasistatic state (as given in (19)), $F_{\text{dev}}^{(2)}(p^\star)$ is the threshold fabric anisotropy, and I_0^F is the typical inertial number, which is an order of magnitude different from I_0^{σ}. Green, red, and black lines show the fit to the preceding relation at pressure levels 100, 200, and 400 Nm^{-2}, respectively, with points in the center of the shear band highlighted (black circles). Fit parameters to these results are presented in table 3. It is noticeable that unlike μ, I alone is not able to describe F_{dev}, with the effect of pressure being prominent in case of slow flows i.e., low I. In contrast, for fast flows, the deviatoric fabric seems to become independent of pressure.

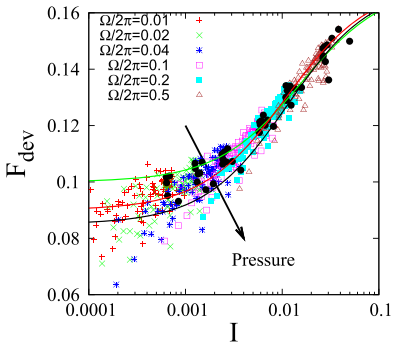

Figure 11. The local fabric anisotropy $F_{\rm dev}$ plotted against the inertial number I for results from simulations with different rates of rotation. Different symbols represent different rates of rotation as given in the legend. Lines are fit to (23) for pressure levels $p = 100,\ 200$, and 400 Nm^{-2} respectively, with fit parameters given in table 3. The arrow shows increasing pressure. Black circles represent the data in the center of the shear band, other data are shown for $\dot{\gamma} > \dot{\gamma}_c = 0.01\ \mathrm{s}^{-1}$.

Table 3. Table showing the fit parameters $F^0_{\rm dev}$, $F^{(2)}_{\rm dev}$, and I^F_0 in (23) for different values of pressure p (in units of Nm^{-2}).

p	F^0_{dev}	$F^{(2)}_{\rm dev}$	I^F_0
100	0.1 ± 0.0005	0.17 ± 0.0005	0.012
200	0.095 ± 0.0008	0.17 ± 0.0001	0.011
400	0.085 ± 0.0001	0.17 ± 0.0004	0.009

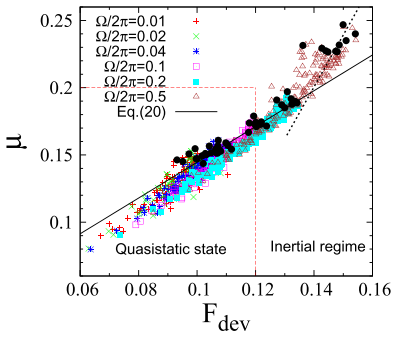

Figure 12. μ plotted against $F_{\rm dev}$ for results from simulations with different rates of rotation, as given in the legend. The solid line represents (20), while the dashed line (with slope $\backsimeq$3.5) is fit by the eye. Black circles represent the data in the center of the shear band, other data are shown for $\dot{\gamma} > \dot{\gamma}_c = 0.01\ \mathrm{s}^{-1}$. The red dashed line separates quasistatic and inertial regimes, based on the data in figure 8.

The increase in the contact anisotropy with inertial number is in accordance with some recent studies [49, 68]. It is important to mention that for even higher rates of rotation of the system, i.e., inertial number $I > 0.1$, $F_{\rm dev}$ shows a different behavior as predicted by (23) and a decreasing trend is observed (as reported in [45]), which is beyond the scope of this work. This might be due to the fact that for $I > 0.1$ the packing becomes very loose ($\nu \leqslant 0.55$). Also for such high rates of rotation, the centrifugal force on grains due to rotation becomes comparable to the gravitational force. As a result, the top surface is not flat anymore; instead the surface develops a dip in the middle, as observed previously [45, 70, 71]. In this range, the kinetic and contact contributions of the local effective friction μ also become comparable.

Starting from both variations of local effective friction and fabric anisotropy as a function of inertial number I, it is tempting to ask the question if the correlation in (20) holds for the inertial regime as well. The result is displayed in figure 12. The solid line shows (20), which fits well the shear band center data being highlighted by black circles. It is noticeable that the fit used by the shear band data in the quasistatic state works well for some range in the inertial regime $I > 0.005$. On the other hand the data outside the shear band shows a different behavior and is found to be below the solid line, which is consistent with the trend observed in case of μ and $F_{\rm dev}$ (separately) as a function of I. However, for even faster flows, a different trend is observed that can also be fitted

by a slightly different linear relation (dot-dashed line). This shows that the effective friction and fabric anisotropy are correlated even in the inertial regime. We check a possible dependence of this correlation on pressure in appendix B, and we find that the correction has no dependence on pressure.

5. Discussion and conclusion

To summarize, this work is an exploration of 3D granular shear flow using DEM particle simulations. We particularly focused on the effect of both particle softness and external compression (gravity) on the flow behavior, considering both local stress and structure as the relevant state parameters.

Quasistatic flows Our study shows that the shear strength (effective macroscopic friction coefficient μ) of the material decreases with increase in either pressure or particle softness for the quasistatic flows, so the $\mu(I)$ rheology has to be generalized. We find that the data for a broad range of pressure (different gravity) and particle softness can be expressed as a unique power law, when analyzed in terms of the control parameter *local dimensionless pressure* p^*, which can be interpreted as the non-dimensional *local* average overlap (scaled with mean particle diameter). This quantity is also a ratio of time scales and can be used to quantify the softness of the bulk material relative to the *local* compression (pressure) level. Low values of p^* signify rigid particles, while a high p^* implies soft, deformable particles. Both softness and pressure are also found to affect the local microstructure, i.e., the anisotropy of the contact network, which is quantified by the deviatoric fabric (F_{dev}). We show that the deviatoric fabric can also be expressed as a power law of p^* with an exponent similar to that of the shear strength but a different characteristic dimensionless pressure. This points out that the local anisotropy of the contact network (deviatoric fabric) and the shear strength of the material are highly correlated in the slow, quasistatic flows and the shear strength follows the anisotropy of the contact network, albeit with a different response characteristics.

These results can be significant for planetary studies regarding the shear strength of the granular material on extraterrestrial bodies such as Moon or Mars. Significant amount of experimental work using parabolic flights have shown the increase in shear strength of the material with decreasing gravity [18–23] without proper explanation. We propose that the anisotropy, i.e., the rearrangement in the contact network, is the key mechanism controlling this dependence if no new g-dependent effects or forces are involved. With decreasing pressure, the packing becomes loose (due to decrease in body force acting on the particles), which in turn provides more free space to the particles to rearrange (and thus align) in response to the local shear. The fact that the particle softness and pressure have been shown to have similar effects on the local flow behavior makes this work equally relevant for *soft particles* that find their applications in many engineering and biological systems [25]. Since it is extremely difficult and expensive to perform *in situ* experiments on the Moon (or even the parabolic flight), the 'compensation' effect we find with the ratio of pressure g and particle stiffness k_n allows us to mimic a variable broad pressure range by tweaking/tuning the particle stiffness. Centrifuges can be used for variation towards larger g, i.e., softer particles.

Even though the shear strength and deviatoric fabric are found to be strongly correlated, we find that the fabric tensor is in an almost planar state like the strain-rate tensor, whereas the stress tensor is in a planar state with a strong additional triaxial component. This shows that even though the norms of two tensors are found to be correlated, still they can behave differently.

Inertial flows Further, to study the rheology of the system for gravity $g = 10\ \mathrm{ms}^{-2}$ and $k_n = 100\ \mathrm{Nm}^{-1}$, the rotation rate of the system is increased. For faster flows the system enters into a rate dependent *inertial regime*, consistent with previous studies [6, 8, 55]. We find that the frictional laws obtained from homogeneous shear flows [55] can be applied locally in the inertial regime, while they fail to predict the behavior of the material in the slower, quasistatic regime, in case of non-homogeneous granular flows. The local rheology laws can be applied to our data in the center of the shear bands, where the strain rate and stress gradients are zero, hence the material can be assumed to be homogeneously sheared. However, away from the center of the shear bands, in the quasistatic regime, we observe a nearly identical range of μ values corresponding to a completely different range of I. We find that in our system the material is able to flow even below μ_0^{local}, albeit slowly; we explain this by using an approach similar to Koval *et al* [9]. The local contact anisotropy (F_{dev}) also shows behavior similar to that of μ_0^{local}, i.e., it increases with increasing I, including some similar, possibly non-local effects. This shows that local effective friction and contact anisotropy are correlated in both quasistatic state and inertial regime. Thus the increase of μ with I as observed in the *inertial regime* is accompanied by the evolution of the microstructure (contact anisotropy) with increasing inertial number. This picture is consistent with the recent study of Azéma *et al* [68]. However, for very fast flows, a different trend is observed.

Conclusion The effective macroscopic friction (steady state shear strength) of the material is found to be affected not only by the local shear rate, but also by external compression (due to pressure) and softness of the particles. While traditionally the inertial number, the ratio of stress and strain-rate time scales, is dominating the

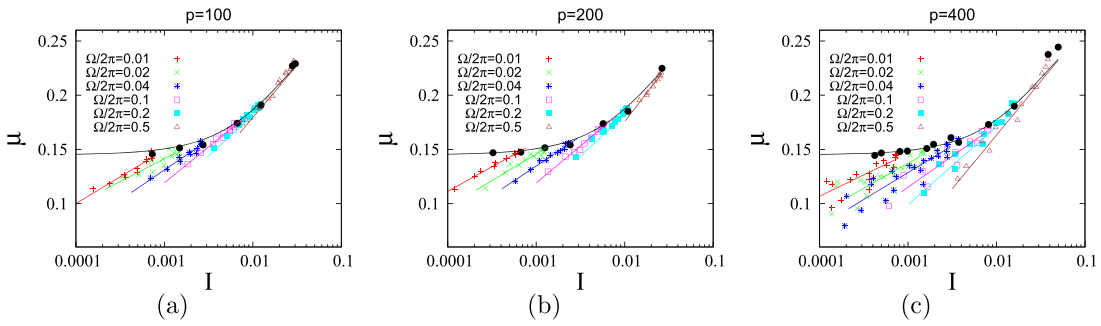

Figure A1. μ plotted against I for different local pressures in the system (a) $p = 100$, (b) $p = 200$, and (c) $p = 400$ Nm^{-2}.

flow rheology, we find that a second dimensionless number, the ratio of softness and stress time scales, must be involved to characterize the bulk flow behavior. For very slow shear rate the former can be ignored, while the latter affects the shear strength by decreasing it with an increase in either gravity (and thus local pressure) or particle softness. For faster flows, the effective friction is found to increase in general with increasing shear rate. However, the tails of shear bands feature an anomalously small effective friction—as observed previously [9, 10, 72]. For the dependence of effective macroscopic friction on the preceding three quantities, the change in local microstructure (contact anisotropy) is found to be a key parameter, with similar norm, but different shape factor.

Open issues The deviations observed in μ_0^{local} for slow flows might also be well captured using the non-local models developed recently by Kamrin *et al* [10, 11, 72]; this work is in progress. Another related issue that remains untouched is the effect of particle softness and external compression (gravity here) on the non-locality. A study of effect of pressure (gravity) on primary and secondary velocity fields, as done recently in [73, 74], also deserves a further study, as well as the effect of softness and pressure on the shear banding. Looking towards the future, we are now in a position to address various important issues, such as unexpectedly high shear strength of the material at low (normal) stress or reduced gravity and a direct relation between the contact anisotropy and the shear strength of the material. These issues are vital for a better explanation of the macroscopic behavior of the granular systems from a macroscopic observation. The current study dealt with a dense system with small interparticle friction ($\mu_p = 0.01$), where the effect of softness on the macroscopic behavior is more direct than for large μ_p. However, an issue that remains unanswered and will be an extension of this study is whether the same effect can also be observed for relatively loose systems (with higher interparticle friction). The question of whether the correlation between contact anisotropy and shear strength is just a consequence of relatively low interparticle friction or if it will also hold for a more realistic material (with higher interparticle friction) remains to be answered. Finally, the influence of polydispersity on our major findings is an open question too.

Acknowledgments

We would like to thank C R K Windows-Yule, D Vescovi, and T Weinhart for their careful revisions. We thank W Losert, D van der Meer, M Sperl, D Lohse, B Tighe, P Jop, H Hayakawa, A Ikeda, O I Imole, and L Silbert for stimulating discussions. Financial support through the Jamming and Rheology project of the Stichting voor Fundamenteel Onderzoek der Materie (FOM), which is financially supported by the Nederlandse Organisatie voor Wetenschappelijk Onderzoek (NWO), is acknowledged.

Appendix A. Pressure dependence of local macroscopic friction

In this section, we explore the pressure dependence of our rheological laws as presented in section 4. Figure A1 shows the fits for three different pressure levels (height in the split-bottom cell), namely close to bottom, mid-height, and top. We find for pressure levels the fitted law (22) well describes the data. Figure A2 shows the fitting parameters α and I^*, versus rotation rate $\Omega/2\pi$ for different pressure levels. Interestingly, we observe that both α and I^* collapse irrespective of pressure value. We conclude that the fitting variables do not depend on pressure, and no extra pressure parameter is required in (22).

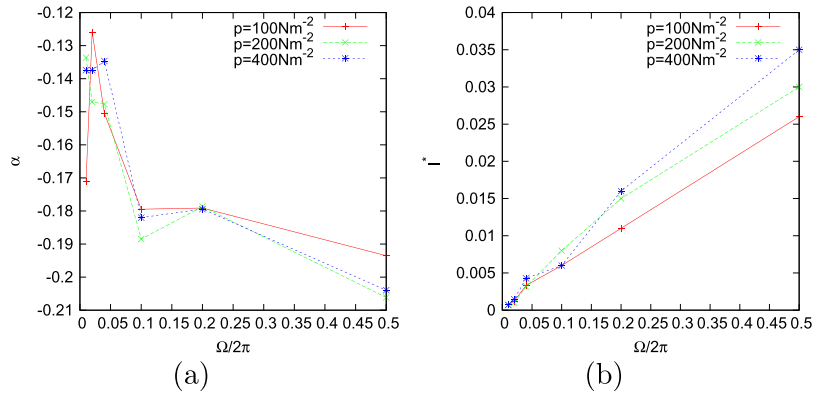

Figure A2. (a) α and (b) I^* plotted against the external rotation rate for different local pressures in the system.

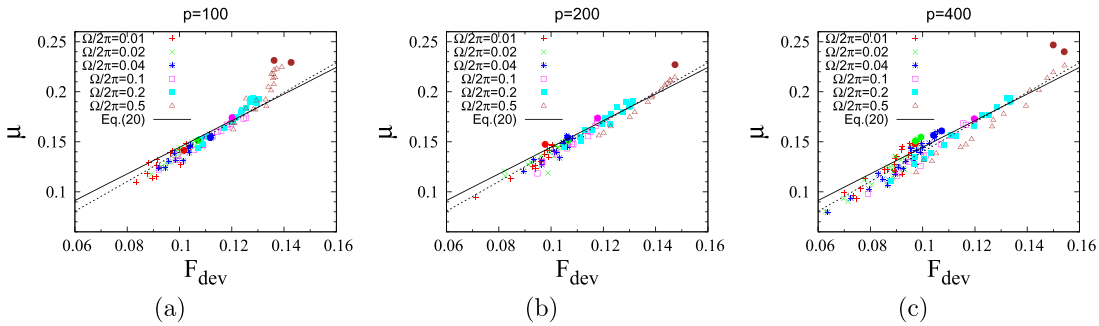

Figure B1. μ plotted against F_{dev} for different local pressures in the system (a) $p = 100$, (b) $p = 200$, and (c) $p = 400$ Nm^{-2}. The solid line represents the corresponding fit as presented in (20), while the dashed line is the best fit to the data.

Appendix B. Pressure dependence of correlation

In this section, we test the correlation between μ and F_{dev} in quasistatic and extended inertial regimes that was presented in section 4. Figure B1 shows the data for three different pressure levels namely close to bottom, mid-height, and top. The solid line shows (20), while the dashed line shows the best fit through the data. We see that the dashed line is below the solid line, which is consistent with the observation in figure 12. The correlation holds very well for all rotation rates, except for the fastest, which seems to fall off from the prediction of (20).

References

[1] Jaeger H M, Nagel S R and Behringer R P 1996 Granular solids, liquids, and gases *Rev. Mod. Phys.* **68** 1259–73
[2] Duran J 2000 *Sands Powders, and Grains-An Introduction to the Physics of Granular Materials* (New York: Springer)
[3] Andreotti B, Forterre Y and Pouliquen O 2013 *Granular Media: between Fluid and Solid* (Cambridge: Cambridge University Press)
[4] Goldhirsch I 2003 Rapid granular flows *Annu. Rev. Fluid. Mech.* **35** 267–93
[5] Nedderman R M 2005 *Statics and Kinematics of Granular Materials* (Cambridge: Cambridge University Press)
[6] MiDi G D R 2004 On dense granular flows *Euro. Phys. J. E.: Soft. Mat. Bio. Phys.* **14** 341–65
[7] Jop P, Forterre Y and Pouliquen O 2006 A constitutive law for dense granular flows *Nature* **441** 727–30
[8] Forterre Y and Pouliquen O 2008 Flows of dense granular media *Annu. Rev. Fluid Mech.* **40** 1–24
[9] Koval G, Roux J-N, Corfdir A and Chevoir F 2009 Annular shear of cohesionless granular materials: from the inertial to quasistatic regime *Phys. Rev.* E **79** 021306
[10] Kamrin K and Koval G 2012 Nonlocal Constitutive Relation for Steady Granular Flow *Phys. Rev. Lett.* **108** 178301
[11] Henann D L and Kamrin K 2013 A predictive, size-dependent continuum model for dense granular flows *Proc. Natl Acad. Sci. USA* **110** 6730–5
[12] Krohn K *et al* 2014 Mass movement on vesta at steep scarps and crater rims *Icarus* **244** 120–32
[13] Shinbrot T, Duong N-H, Kwan L and Alvarez M M 2004 Dry granular flows can generate surface features resembling those seen in Martian gullies *Proc. Natl Acad. Sci. USA* **101** 8542–6
[14] Malin M C 1992 Mass movements on Venus: preliminary results from magellan cycle 1 observations *J. Geophys. Res.: Planets* **97** 16337–52
[15] Howard K A 1973 Avalanche mode of motion: implications from lunar examples *Science* **180** 1052–5

[16] Tardos G I, McNamara S and Talu I 2003 Slow and intermediate flow of a frictional bulk powder in the Couette geometry *Powder Tech.* **131** 23–39
[17] Campbell C S 2002 Granular shear flows at the elastic limit *J. Fluid Mech.* **465** 261–91
[18] Macari-Pasqualino E J, Sture S and Runesson K 1991 Analysis of low effective stress characteristics of granular materials in reduced gravity *Geotechn. Eng. Congress 1991* (ASCE) pp 1222–33
[19] Costes N C, Janoo V C and Sture S 1987 Microgravity experiments on granular materials *Mat. Res. Soc. Symp. Proc.* **87** 203–12
[20] Klein S P and White B R 1990 Dynamic shear of granular material under variable gravity conditions *AIAA J.* **28** 1701–2
[21] Alshibli K A, Sture S and Costes N C 2000 Constitutive and stability behavior of soils in microgravity environment *In Space Tech. App. Int. Forum-2000* vol 504 (New York: AIP) pp 246–52
[22] Alshibli K A, Costes N C and Porter R F 1996 Mechanics of granular materials (MGM) *SPIE's 1996 Int. Symp. Opt. Sci. Eng. Ins.* (International Society for Optics and Photonics) pp 303–10
[23] Sture S, Costes N C, Batiste S N, Lankton M R, AlShibli K A, Jeremic B, Swanson R A and Frank M 1998 Mechanics of granular materials at low effective stresses *J. Aero. Eng.* **11** 67–72
[24] Brucks A, Arndt T, Ottino J M and Lueptow R M 2007 Behavior of flowing granular materials under variable g *Phys. Rev.* E **75** 032301
[25] Hoffman A S 2002 Hydrogels for biomedical applications *Adv. drug delivery rev.* **54** 3–12
[26] Otsuki M, Hayakawa H and Luding S 2010 Behavior of pressure and viscosity at high densities for two-dimensional hard and soft granular materials *Prog. Theor. Phys. Suppl.* **184** 110–33
[27] Makse H A, Johnson D L and Schwartz L M 2000 Packing of Compressible Granular Materials *Phys. Rev. Lett.* **84** 4160
[28] der Vaart K v, Rahmani Y, Zargar R, Hu Z, Bonn D and Schall P 2013 Rheology of concentrated soft and hard-sphere suspensions *J. Rheology (1978-present)* **57** 1195–209
[29] Vescovi D, di Prisco C and Berzi D 2013 From solid to granular gases: the steady state for granular materials *Int. J. Num. Analyt. Meth. Geomech.* **37** 2937–51
[30] Berzi D, di Prisco C and Vescovi D 2011 Constitutive relations for steady, dense granular flows *Phys. Rev.* E **84** 031301
[31] Ries A, Wolf D E and Unger T 2007 Shear zones in granular media: three-dimensional contact dynamics simulations *Phys. Rev.* E **76** 051301
[32] Silbert L E, Grest G S, Brewster R and Levine A J 2007 Rheology and contact lifetimes in dense granular flows *Phys. Rev. Lett.* **99** 068002
[33] Arndt T, Brucks A, Ottino J M and Lueptow R M 2006 Creeping granular motion under variable gravity levels *Phys. Rev.* E **74** 031307
[34] Cundall P A and Strack O D L 1983 Modeling of Microscopic Mechanisms in Granular Materials *Mecha. Gran. Mat.: New Models Constit. Relations* ed J T Jenkins and M Satake (Amsterdam: Elsevier) pp 137–49
[35] Walton O R 1993 Numerical simulation of inclined chute flows of monodisperse, inelastic, frictional spheres *Mech. Mater.* **16** 239–47
[36] Luding S, Lätzel M and Herrmann H J 2001 From discrete element simulations towards a continuum description of particulate solids *Handbook of Conveying and Handling of Particulate Solids* ed A Levy and H Kalman (Amsterdam: Elsevier) pp 39–44
[37] Luding S 2008 Introduction to discrete element methods: basic of contact force models and how to perform the micro-macro transition to continuum theory *Eur. J. Environ. Civil Eng.* **12** 785–826
[38] Luding S 2008 Cohesive frictional powders: contact models for tension *Gran. Matt.* **10** 235–46
[39] Fenistein D and van Hecke M 2003 Kinematics—wide shear zones in granular bulk flow *Nature* **425** 256
[40] Fenistein D, van de Meent J W and van Hecke M 2004 universal and wide shear zones in granular bulk flow *Phys. Rev. Lett.* **92** 094301
[41] Luding S 2008 The effect of friction on wide shear bands *Particulate Science and Technology* **26** 33–42
[42] Dijksman J A and van Hecke M 2010 Granular flows in split-bottom geometries *Soft Matt.* **6** 2901–7
[43] Luding S 2008 Constitutive relations for the shear band evolution in granular matter under large strain *Particuology* **6** 501–5
[44] Singh A, Magnanimo V, Saitoh K and Luding S 2014 Effect of cohesion on shear banding in quasistatic granular materials *Phys. Rev.* E **90** 022202
[45] Singh A 2014 *Micro-macro and Rheology in Sheared Granular Matter* (Enschede: Universiteit Twente)
[46] Moosavi R, Shaebani M R, Maleki M, Török J, Wolf D E and Losert W 2013 Coexistence and transition between shear zones in slow granular flows *Phys. Rev. Lett.* **111** 148301
[47] Bagi K 1999 Microstructural stress tensor of granular assemblies with volume forces *J. Appl. Mech.* **66** 934–6
[48] Lätzel M, Luding S and Herrmann H J 2000 Macroscopic material properties from quasi-static, microscopic simulations of a two-dimensional shear-cell *Gran. Matt.* **2** 123–35
[49] Weinhart T, Hartkamp R, Thornton A R and Luding S 2013 Coarse-grained local and objective continuum description of three-dimensional granular flows down an inclined surface *Phys. Fluids* **25** 070605
[50] Imole O I, Kumar N, Magnanimo V and Luding S 2013 Hydrostatic and shear behavior of frictionless granular assemblies under different deformation conditions *KONA* **30** 84–108
[51] Kumar N, Luding S and Magnanimo V 2014 Macroscopic model with anisotropy based on micro-macro informations *Acta Mech.* **225** 2319–43
[52] Depken M, van Saarloos W and van Hecke M 2006 Continuum approach to wide shear zones in quasistatic granular matter *Phys. Rev.* E **73** 031302
[53] Imole O I, Wojtkowski M, Magnanimo V and Luding S 2014 Micro-macro correlations and anisotropy in granular assemblies under uniaxial loading and unloading *Phys. Rev.* E **89** 042210
[54] Luding S 1998 Collisions & contacts between two particles *Physics of Dry Granular Media* (Berlin: Springer) pp 285–304
[55] da Cruz F, Emam S, Prochnow M, Roux J and Chevoir F 2005 Rheophysics of dense granular materials: discrete simulation of plane shear flows *Phys. Rev.* E **72** 021309
[56] Savage S B 1984 The mechanics of rapid granular flows *Advances in applied mechanics* **24** 289–366
[57] Wortel G H, Dijksman J A and van Hecke M 2014 Rheology of weakly vibrated granular media *Phys. Rev.* E **89** 012202
[58] Wood D M 1990 *Soil Behaviour and Critical State Soil Mechanics* (Cambridge: Cambridge University Press)
[59] Szabó B, Török J, Somfai E, Wegner S, Stannarius R, Böse A, Rose G, Angenstein F and Börzsönyi T 2014 Evolution of shear zones in granular materials *Phys. Rev.* E **90** 032205
[60] Singh A, Magnanimo V and Luding S 2013 Effect of friction and cohesion on anisotropy in quasi-static granular materials under shear (*Powders and Grains, AIP Conf. Proc.* vol 1542) ed A Yu and S Luding pp 682–5
[61] Peyneau P-E and Roux J-N 2008 Frictionless bead packs have macroscopic friction, but no dilatancy *Phys. Rev.* E **78** 011307
[62] Unger T 2010 Collective rheology in quasi static shear flow of granular media (arXiv:1009.3878)
[63] Dorbolo S, Scheller T, Ludewig F, Lumay G and Vandewalle N 2011 Influence of a reduced gravity on the volume fraction of a monolayer of spherical grains *Phys. Rev.* E **84** 041305

[64] Göncü F, Duran O and Luding S 2010 Constitutive relations for the isotropic deformation of frictionless packings of polydisperse spheres *C. R. Mécanique* **338** 570–86
[65] Zhang H P and Makse H A 2005 Jamming transition in emulsions and granular materials *Phys. Rev.* E **72** 011301
[66] Veje C T, Howell D W and Behringer R P 1999 Kinematics of a 2D granular Couette experiment at the transition to shearing *Phys. Rev.* E **59** 739–45
[67] Majmudar T S and Behringer R P 2005 Contact force measurements and stress-induced anisotropy in granular materials *Nature* **435** 1079–82
[68] Azéma E and Radjaï F 2014 Internal structure of inertial granular flows *Phys. Rev. Lett.* **112** 078001
[69] Singh A, Magnanimo V and Luding S 2014 Effect of friction on the force distribution in sheared granular materials *Proc. of NUMGE2014* (Boca Raton, FL: CRC Press) pp 409–14
[70] Dijksman J A *et al* 2009 *Granular media: flow & agitations, Granular and Disordered Media* Leiden Institute of Physics, Faculty of Science, Leiden University
[71] Corwin E I 2008 Granular flow in a rapidly rotated system with fixed walls *Phys. Rev.* E **77** 031308
[72] Kamrin K and Koval G 2014 Effect of particle surface friction on nonlocal constitutive behavior of flowing granular media *Comp. Part. Mech.* **1** 169–76
[73] Murdoch N, Rozitis B, Green S F, Lophem T-L, Michel P and Losert W 2013 Granular shear flow in varying gravitational environments *Gran. Matt.* **15** 129–37
[74] Murdoch N, Rozitis B, Nordstrom K, Green S F, Michel P, de Lophem T-L and Losert W 2013 Granular convection in microgravity *Phys. Rev. Lett.* **110** 018307